

Full length article

Ab initio study of the effect of interstitial alloying on the intrinsic stacking fault energy of paramagnetic γ -Fe and austenitic stainless steel

Frank Niessen ^{a,*}, Wei Li ^{b,c}, Konstantin V. Werner ^a, Song Lu ^b, Levente Vitos ^{b,c,d}, Matteo Villa ^a, Marcel A.J. Somers ^a

^a Department of Civil and Mechanical Engineering, Technical University of Denmark, Kgs. Lyngby 2800, Denmark

^b Applied Materials Physics, Department of Materials Science and Engineering, Royal Institute of Technology, Stockholm SE-100 44, Sweden

^c Department of Physics and Astronomy, Division of Materials Theory, Uppsala University, P.O. Box 516, Uppsala SE-75121, Sweden

^d Research Institute for Solid State Physics and Optics, Wigner Research Center for Physics, P.O. Box 49, Budapest H-1525, Hungary

ARTICLE INFO

Keywords:

Stacking fault energy
Austenitic stainless steel
Density functional theory modeling
Deformation mode
Martensite formation

ABSTRACT

Intrinsic stacking fault energy (SFE) values of γ -Fe and AISI 304 austenitic stainless steels were determined as a function of carbon and nitrogen content using ab initio calculations. In contrast to previous investigations, the analysis was conducted incorporating the paramagnetic state to account for the magnetic constitution of real austenitic stainless steels. The effect of finite temperature was partially accounted for by performing ab initio calculations at the experimental volumes at room temperature. Including paramagnetism in γ -Fe increases the SFE of *non-magnetic* γ -Fe by $\sim 385 \text{ mJ.m}^{-2}$. Interstitial alloying of *non-magnetic* γ -Fe causes a linear increase in intrinsic stacking fault energy with interstitial content. In comparison, interstitial alloying of *paramagnetic* γ -Fe increases the SFE at only about half the rate. The SFE of *paramagnetic* interstitial-free AISI 304 is within the range of -12 to 0 mJ.m^{-2} and only deviates slightly from the SFE of *paramagnetic* γ -Fe. It follows a similar, albeit flatter linear dependency on the interstitial content compared to γ -Fe. Both γ -Fe and γ -AISI 304 were found to be metastable in their interstitial-free condition and are stabilized by interstitial alloying. The possible effect of short range ordering between interstitials and Cr on the SFE was discussed. The calculated threshold nitrogen content necessary to stabilize austenite in AISI 304 is in good agreement with experimental investigations of deformation microstructures in dependence of the nitrogen content. Finally, the calculated negative SFE values of AISI 304 were reconciled with experimentally determined positive SFE values using a recent method that accounts for the kinetics of stacking fault formation.

1. Introduction

The stacking fault energy (SFE) is a prominent materials property in face-centered cubic (*fcc*) metals and alloys that is considered to control the activation of different (combinations of) deformation modes. A pragmatic classification uses SFE to subdivide regimes of deformation modes: dislocation glide and ϵ -martensite formation occur for $\text{SFE} < 20 \text{ mJ.m}^{-2}$, dislocation glide and mechanical twinning for $\text{SFE} \sim 20\text{--}40 \text{ mJ.m}^{-2}$ and only dislocation glide for $\text{SFE} > 40 \text{ mJ.m}^{-2}$ [1]. As the design of new advanced high-strength steels and high-entropy alloys focusses on the activation of multiple deformation modes to obtain high ductility and toughness at high strength, SFE is considered to be the decisive design parameter for the discovery of new alloys with unique mechanical properties [2–7]. Experimental methods for SFE determination rely

on assessing the separation distance between Shockley partial dislocations which frame a stacking fault, assuming that the force stored in the SF is balanced by the repulsive forces among the Shockley partials. Recently, it has been brought forward that the separation of the Shockley partials is also affected by other forces such as lattice friction [8–11] and imaging forces from finite grain size [12–15] that play a role during SF formation. Since such kinetic effects are not accounted for in the “equilibrium force” definition of the experimental SFE, the determined SFE is biased and gives fundamentally different values from the SFE obtained via ab initio thermodynamics [10]. This is especially prominent for the group of metastable *fcc* alloys, which are associated with low SFE and therefore experience a relatively strong effect of the kinetics contribution [8,10,11,16].

Theoretical methods to determine SFE values include CALPHAD [17]

* Corresponding author.

E-mail address: frannie@dtu.dk (F. Niessen).

and ab initio [18,19] thermodynamics modeling. CALPHAD-based methods [20–24] commonly calculate the SFE using the Olson-Cohen model [25], in which a stacking fault is portrayed as a hexagonal close packed (*hcp*) double-layer, representing an ϵ martensite embryo. The model considers the *fcc*-to-*hcp* driving force and the interfacial energy as the major contributions to the SFE. The latter cannot be obtained from CALPHAD-based methods directly and is therefore approximated [20,21,24,26] or used as a fitting parameter [22,23]. Fitting of the interfacial energy often leads to quite large values (e.g. up to 32.5 mJ.m⁻² in Ref. [23]), while ab initio methods have shown that this value is in the range of -9 to 9 mJ.m⁻² [27]. Another drawback of CALPHAD approaches is that the Gibbs energies at low temperatures, especially for metastable phases, such as *hcp* ϵ phase in steel [28], are not accurate in thermodynamics databases, causing high uncertainties [24,29]. Thermodynamics models that specifically focus on SFE prediction commonly compensate for the database inaccuracies by a selective compilation [20–24] or fitting [21] of thermodynamics parameters with the aim of finding best possible agreement with experimentally determined SFE values. Considering the recently discussed shortcomings of experimental methods to determine the SFE [8–10], it needs to be questioned whether this type of validation of CALPHAD-based methods is meaningful.

There are two major approaches for the calculation of SFEs from ab initio methods: (i) the axial interaction model [30,31], where the first-order term is equivalent to the above described Olson-Cohen model when neglecting the interfacial energy [25], and (ii) explicit modeling of the stacking fault in a supercell [32]. Besides the *fcc*-to-*hcp* driving force, the latter approach also directly yields the contribution of the interfacial energy to the SFE. Unlike CALPHAD-based methods, ab initio methods do not rely on experimental data to determine SFE values. Rather, ab initio methods compute the internal energy (or total energy) for the ground state, thereby neglecting other energy contributions such as electronic, vibrational, magnetic, and explicit anharmonic contributions. These contributions can be accounted for by including additional models [33–35], which is particularly relevant for finite-temperature calculations. Ab initio methods, most prominently Density Functional Theory (DFT) models [18,19], have been successfully applied to map the change in SFE induced by the variation in substitutional alloying elements in steels, for instance for Cr [36,37], Ni [36–38], Mn [39–42], Al [39,41] and Si [41].

Understanding the effect of substitutional elements on SFE is crucial, but the design of advanced high-strength steels relies importantly on the interstitial alloying elements carbon and nitrogen. These interstitials are the most cost-efficient way of stabilizing *fcc* austenite (γ) phase and are the most efficient solid-solution strengtheners [43]. Unfortunately, from experimental work on identifying the effect of interstitial alloying on SFE, an inconsistent picture emerges, which is likely related to the previously mentioned shortcomings of experimental SFE determination. It has been reported that alloying with carbon leads to an increase in SFE [44–50], little to no effect on SFE [51–53], or a non-linear effect [54, 55]. Analogously, for alloying with nitrogen, an increasing [56–60], a decreasing [44,48,61,62], little to no [52], or a non-linear effect [53, 63–65] on the SFE have been reported.

There is only a handful of ab initio studies on the effect of interstitial alloying on the SFE of γ -Fe [39,40,66–69]. Apart from one study [69], all assume Fe as *non-magnetic*. The results from these studies are in good agreement with each other and report that pure γ -Fe has a SFE of ~ 400 mJ.m⁻² and that the addition of one interstitial atom per 100 Fe atoms increases this value by ~ 70 mJ.m⁻². However, γ -Fe and many of its alloys are paramagnetic under ambient conditions and neglecting the paramagnetic state severely affects the dependence of SFE on composition [40,70].

In the present work, for the first time, ab initio calculations are performed to systematically describe the effect of carbon and nitrogen alloying on the SFE in *paramagnetic* γ -Fe and AISI 304 austenitic stainless steels. The results are discussed in the light of experimental observations on the transformation behavior of AISI 304 and are reconciled with

experimental SFE values.

2. Computational methods

2.1. Calculation of stacking fault energies

The effect of interstitial alloying with carbon and nitrogen on the intrinsic SFE of Fe and AISI 304 austenitic stainless steels was analyzed using DFT modeling [18,19]. The intrinsic SFE, γ_{isf} , was approximated by the first-order term of the axial interaction model [30,31,36]:

$$\gamma_{isf} = 2(F_{hcp} - F_{fcc}) / A \quad (1)$$

where F_{hcp} and F_{fcc} are the Helmholtz energies per atom of the *hcp* and *fcc* crystal structures, and A is the area of the stacking fault per atom. Abbasi et al. [68] and Lu et al. [69] demonstrated that SFE values obtained with the axial interaction model are in close agreement with averaged SFE values from supercells with different distances of carbon atoms to the stacking fault. Considering the complication of locally relaxing the lattice at the interstitial site and the stacking fault in an explicit supercell setup, we therefore limit ourselves to SFE as determined with the axial interaction model. The Helmholtz energies at room temperature, $T = 293$ K, for each phase were approximated considering the total energy, E , and the magnetic entropy, F_{mag} , at experimentally determined atomic volumes, $V(T)$:

$$F(V, T) = E(V(T)) + F_{mag}(\mu_{ij}(V(T)), T) \quad (2)$$

F_{mag} is a function of T and the local magnetic moments μ_{ij} of atoms of type i at lattice sites of type j , with atomic fraction, x_{ij} , and was approximated by a mean field expression which is valid for completely disordered localized moments [71]:

$$F_{mag} = -TS_{mag} = -k_B T \sum_i \sum_j x_{ij} \ln(1 + \mu_{ij}(V(T))) \quad (3)$$

where k_B is Boltzmann's constant. Additional information on the treatment of the paramagnetic state is given in Section 2.3.

The contributions of the vibrational energy and the electronic entropies to the SFE at ambient conditions were previously shown to be small [70,72]. The dependence of SFE on temperature is affected mostly by the thermal lattice expansion [73–75], which is accounted for by conducting total energy calculations at the experimentally determined atomic volumes at room temperature. The dependence of γ_{isf} on the occupancy of the lattice formed by octahedral interstices y was fitted with linear regression using the *linregress* module in *scipy* [76]. For close-packed lattices, the interstitial occupancy y equals the number of interstitial atoms per substitutional atom.

2.2. Ab initio methods

All calculations were carried out using the coherent potential approximation (CPA) [77,78] as implemented in the exact muffin-tin orbitals (EMTO) package [78,79] applying the Perdew-Burke-Ernzerhof (PBE) [80] exchange-correlation approximation. The radii of the Wigner-Seitz spheres of carbon and nitrogen were optimized, leading to a reduction of 23% compared to the substitutional elements. For nitrogen, $2p$ and $2s^2$ were considered as valence states.

The atomic volumes at room temperature in dependence of the carbon and nitrogen content were obtained from the experimentally determined relationships for strain-free γ -iron by Cheng et al. [81]:

$$\begin{aligned} a_0(y_C) &= 3.573 + 0.0080 y_C [\text{\AA}] \\ a_0(y_N) &= 3.573 + 0.0072 y_N [\text{\AA}] \end{aligned} \quad (4)$$

For austenitic stainless steel, the relationship for AISI 316 by Hummelshøj et al. [82] was employed:

$$a_0(y_{C/N}) = 3.5965 + 0.006029 y_{C/N} [\text{\AA}] \quad (5)$$

The c/a ratios of *hcp* iron and AISI 304 in the interstitial-free condition were optimized at the ground-state volume in the PM state. They were 1.594 and 1.616, respectively, and kept constant for all interstitial contents. Interstitial doping of *fcc* with carbon and nitrogen was modelled by placing a single interstitial atom in an octahedrally coordinated interstice of the *fcc* and *hcp* supercells. The initial *fcc* supercell consisted of 32 substitutional atoms arranged as $2 \times 2 \times 2$ *fcc* unit cells with respect to the *a*, *b* and *c* lattice vectors. The interstitial occupancy was varied by extending the supercell along lattice vector *c* by single unit-cell lengths to yield $2 \times 2 \times 3$, $2 \times 2 \times 4$ and $2 \times 2 \times 5$ supercells, containing 48, 64 and 80 substitutional atoms, respectively. Likewise, the initial *hcp* supercell consisted of 32 substitutional atoms and its *a*, *b*, and *c* vectors were $\sqrt{3}a_{hcp}[1\bar{1}00]$, $a_{hcp}[1\bar{1}\bar{2}0]$, and $2c_{hcp}[0001]$, respectively. As for the *fcc* supercells, the *hcp* supercells were extended along the *c* vector to yield supercells containing 48, 64 and 80 substitutional atoms. Examples of the applied supercells are depicted in Fig. 1 and detailed descriptions of the supercell parameters are tabulated with the results in Section 3.

The 1st coordination shells of the interstitial atoms in the *fcc* and *hcp* lattices (golden atoms in Fig. 1) were manually relaxed for the $2 \times 2 \times 2$ *fcc* and *hcp* supercells at their room temperature atomic volumes by displacing the 1st coordination shells linearly in the radial direction away from the interstitial atom. The EMTO model does not allow for automated ionic relaxation and manual relaxation led to the loss of crystal symmetry. The relaxations were conducted for iron and AISI 304 in the non-magnetic and paramagnetic states. For *fcc*, the relaxation led to an 8.00% increase in distance between interstitial atom and the first coordination shell, which is in excellent agreement with previously reported results for carbon [69]. For *hcp*, this distance was increased by 6.75%. The displacement of the 1st coordination shell was applied to all interstitially occupied supercells. The obtained relaxation parameters were identical for iron and AISI 304, as well as for carbon and nitrogen, and unaffected by the considered magnetic state. Ponomareva et al. [83] showed that the local relaxation induced by the presence of an interstitial atom only strongly affected the first coordination shell and that it had almost no effect on the third shell. Even though the relaxation distance in both structures is known to decrease slightly with increasing volume, its effect is small and is therefore neglected [69]. It was ensured that the k-point density in each supercell affected the calculated SFE by less than 0.01 mJ.m⁻².

In addition to the supercell calculations, the SFE was also determined from the Helmholtz energies of the *fcc* and *hcp* primitive cells of iron and AISI 304 as a function of the volume change associated with interstitial alloying. In comparison to the volume-chemistry-driven effect of

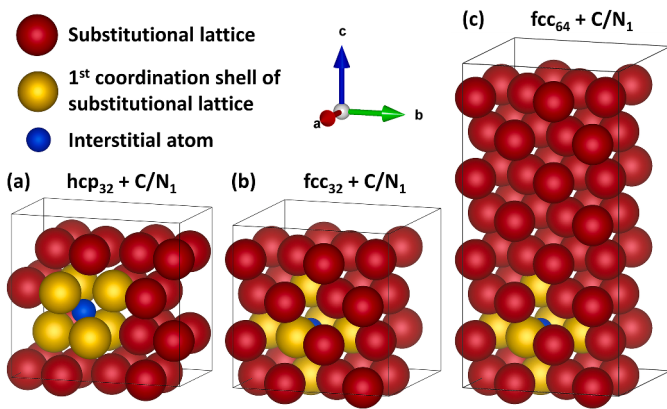


Fig. 1. Representative supercells applied for the SFE calculation with DFT: (a) *hcp*₃₂ + C/N₁, (b) *fcc*₃₂ + C/N₁, and (c) *fcc*₆₄ + C/N₁. The golden atoms mark the 1st coordination shell of the interstitial atom on the octahedral site.

interstitial alloying on SFE, the primitive cells yield a purely volume-driven effect. These SFE values serve as a baseline to highlight the effect of only the volume change. Equivalent calculations were previously used by Molnár et al. [84] to approximate the SFE of nitrogen-alloyed steels.

2.3. Modeling of the paramagnetic state

The paramagnetic (PM) state was modelled using the disordered local magnetic moment (DLM) model [85]. The DLM model is a static model in which both magnetic short and long range ordering are approximated to be zero. Magnetic disorder is modeled by splitting the composition on each sublattice in half and applying non-vanishing and mutually opposing local magnetic moments μ_i and $-\mu_i$ to the respective compositional subsets. The resulting magnetic entropy contribution, F_{mag} , is given in Eq. (3) and its contribution to the SFE scales with the difference in magnetic moments between *fcc* and *hcp*. While not captured by the DLM model, the effect of longitudinal spin fluctuations at ambient conditions is not negligible in γ -Fe and γ -Fe-based alloys [86]. The magnetic moment from longitudinal spin fluctuations in the *hcp* lattice is larger than the one in the *fcc* lattice. The contribution from longitudinal spin fluctuations would make up for the in overall lower static magnetic moment of *hcp* with respect to *fcc* lattice and therefore results in a lower contribution of the magnetic entropy F_{mag} to the SFE [87,88]. To take the effect of longitudinal spin fluctuations at ambient temperature into account, we report both SFE values with and without consideration of F_{mag} and consider that the true ab initio SFE values lie in between these SFE values.

3. Results and interpretation

3.1. SFE of non-magnetic Fe-C and Fe-N systems

In Fig. 2 values for γ_{isf} from ab initio for the different non-magnetic Fe_xC/N₁ compositions, listed in Table 1, are compared with DFT-calculated values of γ_{isf} from literature. The data shows a negative γ_{isf} value of -388.3 mJ.m^{-2} for pure non-magnetic γ -Fe. γ_{isf} depends linearly on the occupancy of octahedral interstices with carbon or nitrogen, *y*; the slopes for carbon and nitrogen are 7069 mJ.m^{-2} and 7154 mJ.m^{-2} , indicating a steep dependence. The γ_{isf} values for the same level of interstitial alloying with carbon and nitrogen were equal within $\pm 3 \text{ mJ.m}^{-2}$. These obtained values are in close agreement with the γ_{isf} values computed for non-magnetic Fe_xC₁ compositions by Abbasi et al. [68]. Their γ_{isf} calculations were conducted at the ground state volumes using the Vienna ab initio simulation package (VASP) [89,90] with the model from Eq. (1) and resulted in a γ_{isf} vs. *y* slope of 6706 mJ.m^{-2} . Their γ_{isf} values were consistently offset by $\sim -40 \text{ mJ.m}^{-2}$ with respect to the present result. Kibey et al. [66] computed γ_{isf} values of Fe_xN₁ using VASP and a Korringa, Kohn and Rostoker (KKR) [91,92] CPA code. Our γ_{isf} value for pure non-magnetic γ -Fe coincided exactly with the γ_{isf} value obtained with the KKR-CPA code, a DFT formulation that is closely related to EMTO. The γ_{isf} values for *y_N* = 0.04 and 0.08 reported by Kibey et al. were 108 and 28 mJ.m⁻² larger than our extrapolated values, respectively. Overall, our values lie in-between the γ_{isf} values for non-magnetic Fe_xC₁ from Abbasi et al. [68] and for Fe_xN₁ from Kibey et al. [66], which validates the supercell setup and DFT parameters applied in this work.

The SFE was also calculated for the *fcc* and *hcp* primitive cell of non-magnetic Fe, considering only the volume-driven effect on SFE, and is plotted as a function of *y* in Fig. 2. The slope of SFE vs. *y* is 531 mJ.m^{-2} with $R^2 = 0.999$ and thereby ~ 13.3 times lower compared to the volume-chemistry-driven effect stated in Table 1. This indicates a major effect of interstitial alloying on the SFE and only a minor effect of the overall volume expansion induced by interstitials.

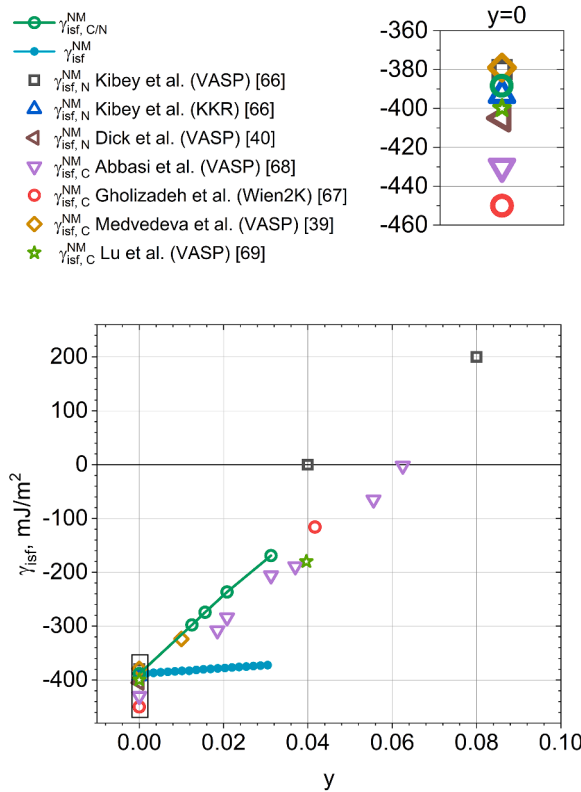


Fig. 2. γ_{isf} of non-magnetic Fe-N and Fe-C alloys vs. the interstitial occupancy, y . The results are compared with DFT-calculated SFE values of non-magnetic Fe-N and Fe-C alloys from literature. $\gamma_{\text{isf}, \text{C}/\text{N}}^{\text{NM}}$ is obtained from supercells, that are explicitly alloyed with interstitials (see Fig. 1) and $\gamma_{\text{isf}}^{\text{NM}}$ from γ -Fe primitive cells that only account for the volume effect caused by interstitial alloying. $\gamma_{\text{isf}, \text{C}}^{\text{NM}}$ and $\gamma_{\text{isf}, \text{N}}^{\text{NM}}$ in this work were identical within 3 mJ.m^{-2} . Values at $y = 0$ are magnified in the inset.

3.2. SFE of paramagnetic Fe-C and Fe-N systems

The calculations from Section 3.1 for non-magnetic $\text{Fe}_x\text{C}/\text{N}_1$ supercells were extended by applying the DLM method to obtain γ_{isf} values for the paramagnetic state. The results are listed in Table 1 and plotted in Fig. 3. The SFE value of paramagnetic γ -Fe increased by 376–391 mJ.m^{-2} with respect to non-magnetic γ -Fe. The contribution of the magnetic entropy F_{mag} to γ_{isf} is initially 15 mJ.m^{-2} and reduces to ~ 5 mJ.m^{-2} at the maximum interstitial occupancy of $y = 0.031$. In contrast

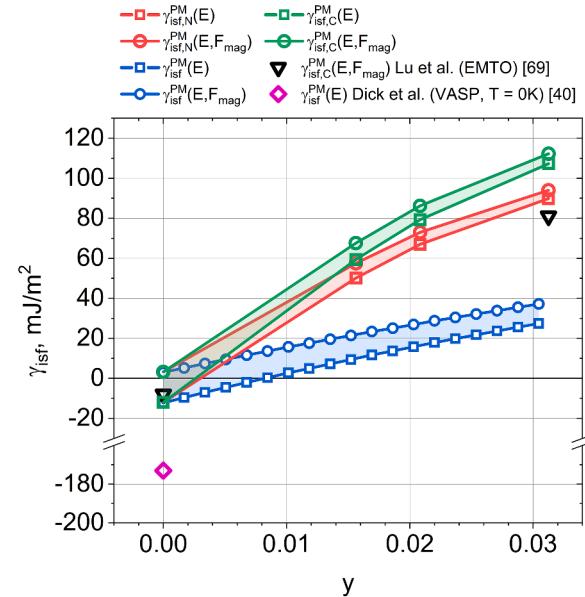


Fig. 3. γ_{isf} of paramagnetic Fe-C and Fe-N alloys vs. the interstitial occupancy, y , compared to values from literature. $\gamma_{\text{isf}, \text{C}}^{\text{PM}}$ and $\gamma_{\text{isf}, \text{N}}^{\text{PM}}$ are obtained from supercells, that contain carbon and nitrogen, respectively (see Fig. 1). $\gamma_{\text{isf}}^{\text{PM}}$ applies for γ -Fe primitive cells that only account for the volume effect caused by interstitial alloying. The discrepancy between γ_{isf} of Dick et al. [40] and the remaining data at $y = 0$ is caused by different choices in volume for the DFT calculations. The true ab initio SFE values are considered to lie within the SFE ranges demarcated by $\gamma(E)$ and $\gamma(E, F_{\text{mag}})$.

to the non-magnetic calculations in Section 3.1, carbon and nitrogen alloying show distinct, yet similar effects on the SFE in the paramagnetic state. Compared to the non-magnetic systems, the slopes of the SFE in the paramagnetic Fe-C and Fe-N systems with interstitial content were reduced by 50% and 59%, respectively. The SFE values of γ -Fe without and with magnetic entropy contributions are -12 and 3 mJ.m^{-2} . Considering the average of these SFE values, the stable-to-metastable transition is observed at an occupancy of 0.0011 (~ 0.028 wt%).

The data by Lu et al. [69] is the only available data for DFT-calculated γ_{isf} values of paramagnetic γ -Fe-C alloys. The dataset contains one point for interstitial-free Fe and one point at $y_C = 0.0313$; both were computed for the same volumes as in our calculation and their results are in excellent agreement with the values obtained in this work. Dick et al. [40] computed γ_{isf} for paramagnetic interstitial-free γ -Fe with VASP at the ground state volume by averaging over several supercells with randomly initialized magnetic moments. Their value for γ_{isf}

Table 1

Details on the DFT-computed SFE of non-magnetic and paramagnetic Fe-N and Fe-C alloys. y is the interstitial occupancy, a_0 is the lattice parameter of the fcc unit cell, x_C and x_N the carbon and nitrogen contents in wt%, and γ_{isf} the intrinsic SFE. NM and PM indicate the non-magnetic and paramagnetic states, respectively. The slopes describe the change in γ_{isf} with y .

Alloy	Fe_{32}	Fe_{80}N	Fe_{64}N	Fe_{48}N	Fe_{32}N	Slope (R^2)
Unit cells	$2 \times 2 \times 2$	$2 \times 2 \times 5$	$2 \times 2 \times 4$	$2 \times 2 \times 3$	$2 \times 2 \times 2$	
y [1]	0	0.0125	0.0156	0.0208	0.0313	
$a_0(y_C)$ [\AA]	3.573	3.583	3.586	3.590	3.598	
x_C [wt%]	0	0.268	0.334	0.445	0.669	
$\gamma_{\text{isf}, \text{C}}^{\text{NM}}(E)$ [mJ.m^{-2}]	-388.3	-295.0	-271.7	-235.0	-168.0	7069 (0.9983)
$\gamma_{\text{isf}, \text{C}}^{\text{PM}}(E)$ [mJ.m^{-2}]	-12.0	-	59.4	79.3	107.3	3845 (0.9832)
$\gamma_{\text{isf}, \text{C}}^{\text{PM}}(E, F_{\text{mag}})$ [mJ.m^{-2}]	3.2	-	67.6	86.2	112.3	3538 (0.9839)
$a_0(y_N)$ [\AA]	3.573	3.582	3.584	3.588	3.596	
x_N [wt%]	0	0.313	0.390	0.519	0.779	
$\gamma_{\text{isf}, \text{N}}^{\text{NM}}(E)$ [mJ.m^{-2}]	-388.3	-297.8	-274.2	-236.5	-169.0	7154 (0.9987)
$\gamma_{\text{isf}, \text{N}}^{\text{PM}}(E)$ [mJ.m^{-2}]	-12.0	-	50.2	67.0	89.9	3823 (0.9601)
$\gamma_{\text{isf}, \text{N}}^{\text{PM}}(E, F_{\text{mag}})$ [mJ.m^{-2}]	3.2	-	57.5	73.0	94.0	2949 (0.9813)

deviates significantly by $\sim -160 \text{ mJ.m}^{-2}$ from the present and Lu et al.'s values. Calculations of SFE vs. volume by Lu et al. [69] however show that the SFE is extremely sensitive to the assumed volume. Lu et al.'s SFE values at the ground state volume are in excellent agreement with the data by Dick et al. [40]. The observed discrepancy is therefore caused by different assumptions for the volumes.

The volume-driven effect of interstitial alloying on SFE was also determined for paramagnetic Fe and is plotted vs. y in Fig. 3. The slopes of SFE vs. y considering the total energy as well as the total energy and the magnetic entropy are 1298 mJ.m^{-2} and 1119 mJ.m^{-2} , respectively, with $R^2 > 0.997$. These slopes are 2.7 to 3.2 times lower compared to the slopes of the volume-chemistry-driven effect.

Fig. 4 shows the magnetic moment of Fe as a function of volume and interstitial content. The plots distinguish the behavior of the six Fe atoms in the 1st coordination shell of the interstitial atom (Fig. 1) and the remaining Fe atoms, which are referred to as the bulk. These magnetic moments are compared with the magnetic moment of Fe primitive cells as a function of volume. It is evident that interstitial alloying leads to a significant reduction in the atomic spin of Fe in the 1st coordination shell and an increase in magnetic moment in the bulk with respect to interstitial-free Fe. These observations are in excellent agreement with previous results from Lu et al. [69] and Ponomareva et al. [83]. The reduction in atomic spin of Fe in the vicinity of carbon and nitrogen has been attributed to several mechanisms: (i) the local volume reduction induced by the lattice distortion around the interstice reduces the atomic spin, as evident from the dependence of magnetic moment in pure Fe vs. volume (Fig. 4) [69], (ii) carbon and nitrogen tend to form covalent bonds with Fe, reducing atomic spin [93,94], and (iii) predominantly

ferromagnetic Fe clusters may form around carbon in the temperature range of overcooled austenite, which was associated with magnetic frustration and reduced atomic spin [83].

The reduction in SFE induced by the magnetic entropy term F_{mag} is caused by a relatively lower magnetic moment of Fe in *hcp* with respect to *fcc*. This difference appears to become less pronounced for increasing volume and interstitial content. As discussed in Section 2.3, the contribution of longitudinal spin fluctuations would somewhat reduce this observed difference in magnetic spin and thereby lower the magnetic entropy contribution to the SFE. Fig. 4 suggests that the lower SFE for nitrogen-alloyed Fe, as compared to carbon-alloyed Fe, is mostly caused by the local magnetic interaction of the Fe lattice with the interstitial atom in the 1st coordination shell. Here nitrogen alloying induces the same magnetic moment in the 1st coordination shell of the *fcc* and *hcp* structures, whereas carbon alloying shows reduced magnetic interaction in the *hcp* structure compared to the *fcc* structure.

3.3. SFE of paramagnetic interstitially alloyed AISI 304

The calculations from Section 3.2 on γ -Fe were extended by assuming the substitutional composition of the AISI 304 in the experimental study by Wang et al. [95]: Fe-18.1Cr-7.9Ni-1.1Mn-0.54Si-0.058C-0.024 N wt %; the carbon and nitrogen contents were varied. The results are listed in Table 2 and are plotted in Fig. 5. As for paramagnetic γ -Fe, nitrogen alloying of AISI 304 leads to an approximately linear increase in SFE. Interstitial-free AISI 304 has a SFE of -12 to 0 mJ.m^{-2} and the slope of SFE vs. carbon and nitrogen occupancy is reduced by $\sim 10\%$ with respect to paramagnetic γ -Fe (Table 2). As the magnetic moment of Fe and Mn in

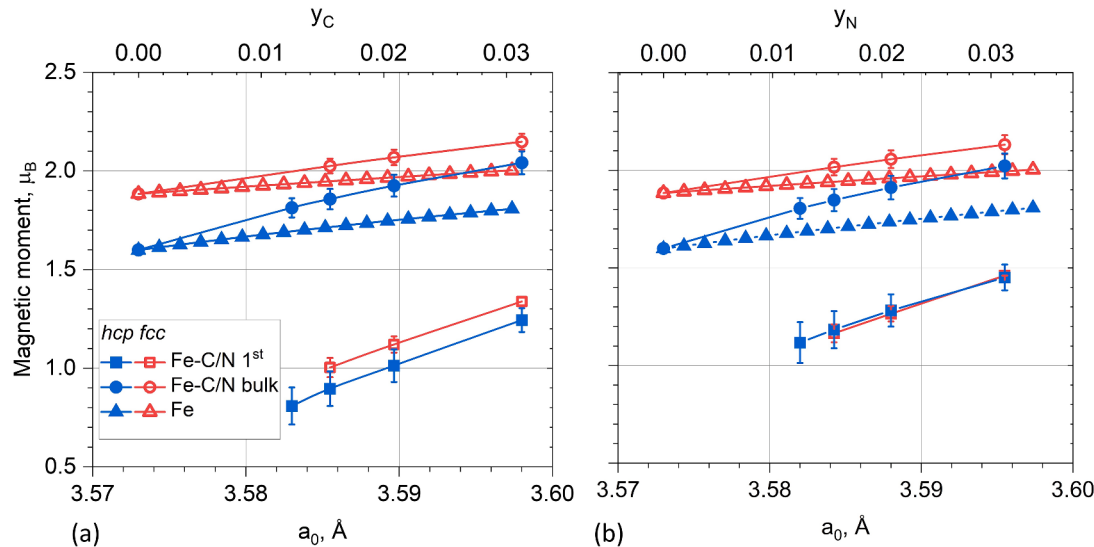


Fig. 4. Magnetic moment of Fe in *fcc* and *hcp* for (a) carbon and (b) nitrogen alloyed supercells. Data compares the mean magnetic moment of the six Fe atoms in the 1st coordination shell of the interstitial atom (see Fig. 1) and of the remaining bulk atoms with the magnetic moment of the interstitial-free Fe primitive cell. The error bars indicate the standard deviation of the magnetic moments of the considered groups of atoms.

Table 2

Details on the DFT-computed SFE of paramagnetic AISI 304-C/N alloys. The legend to the symbols is given in the caption to Table 1.

Alloy	AISI 304 ₃₂	AISI 304 ₆₄ N	AISI 304 ₄₈ N	AISI 304 ₃₂ N	Slope (R^2)
Unit cells	$2 \times 2 \times 2$	$2 \times 2 \times 4$	$2 \times 2 \times 3$	$2 \times 2 \times 2$	
y [1]	0	0.0156	0.0208	0.0313	
$a_0(y_{C/N})$ [Å]	3.5965	3.6059	3.6091	3.6153	
x_C [wt%]	0	0.340	0.453	0.680	
x_N [wt%]	0	0.396	0.527	0.792	
$\gamma_{isf,C}^{PM}(E)$ [mJ.m^{-2}]	-12.3	47.5	65.7	95.5	3483 (0.9942)
$\gamma_{isf,C}^{PM}(E, F_{mag})$ [mJ.m^{-2}]	-0.1	56.2	74.2	101.5	3282 (0.9929)
$\gamma_{isf,N}^{PM}(E)$ [mJ.m^{-2}]	-12.3	41.2	57.5	83.3	3090 (0.9940)
$\gamma_{isf,N}^{PM}(E, F_{mag})$ [mJ.m^{-2}]	-0.1	49.0	64.2	88.2	2853 (0.9932)

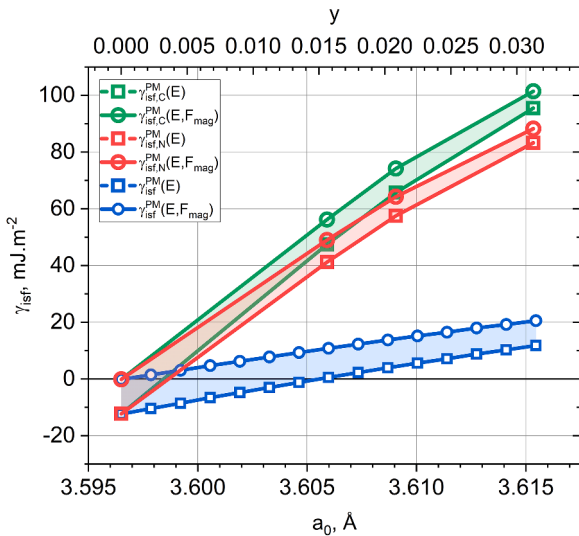


Fig. 5. SFE of paramagnetic AISI 304_xC/N₁ vs. fcc lattice parameter, a_0 , and interstitial occupancy, y . $\gamma_{\text{isf}, \text{C}}^{\text{PM}}$ and $\gamma_{\text{isf}, \text{N}}^{\text{PM}}$ are obtained from supercells, that are explicitly alloyed with carbon and nitrogen, respectively, (see Fig. 1). $\gamma_{\text{isf}}^{\text{PM}}$ applies for interstitial-free AISI 304 primitive cells that only account for the volume effect caused by interstitial alloying. The true ab initio SFE values are considered to lie within the SFE ranges demarcated by $\gamma(E)$ and $\gamma(E, F_{\text{mag}})$.

hcp is consistently lower than in *fcc*, the consideration of F_{mag} leads to a reduction in SFE (Fig. 6 and Fig. 7). The contribution of F_{mag} to the SFE values is initially 12 mJ.m⁻² and reduces to ~5 mJ.m⁻² at $y = 0.031$. Nitrogen as an interstitial species induces a larger magnetic moment in Fe and Mn compared to carbon. Carbon introduces a larger gap in magnetic moment between *fcc* and *hcp* than nitrogen. Considering the mean value of the SFE values $\gamma_{\text{isf,C/N}}^{\text{PM}}(E)$ and $\gamma_{\text{isf,C/N}}^{\text{PM}}(E, F_{\text{mag}})$, the γ phase of AISI 304 transitions from metastable to stable at an interstitial occupancy $y=0.0016$ ($\cong 0.04$ wt%).

The SFE was also calculated for the *fcc* and *hcp* primitive cell of paramagnetic AISI 304 and is plotted as a function of y in Fig. 5 considering no direct C/N-doping but only the effect of volume expansion. The results also show an increase in SFE vs. y , albeit at an approximately three times lower rate. For this approach, the metastable-to-stable transition of the γ phase occurs at a nitrogen occupancy of 0.0037 (=0.094 wt%).

4. Discussion

The SFE values obtained from DFT show that interstitial alloying of non-magnetic and paramagnetic γ -Fe, as well as paramagnetic AISI 304, consistently leads to an increase in SFE. The calculations for non-magnetic interstitially alloyed Fe were in excellent agreement with ab initio calculated SFE values reported in the literature [39,40,66–68]. Including a paramagnetic rather than a non-magnetic state led to an increase in SFE by ~385 mJ.m⁻², which emphasizes the importance of including the magnetic state in DFT calculations. The changes in SFE in paramagnetic γ -Fe with increasing carbon and nitrogen content are also in excellent agreement with data from Lu et al. [69] on Fe and Fe₃₂C₁ and with data by Dick et al. [40] on Fe, provided that the different choice in volume is accounted for. After validation of the simulation setup, paramagnetic Fe was replaced by the metallic composition of AISI 304 (Table 2) to, for the first time, calculate SFE values in this alloy as a function of interstitial content. The results obtained with the axial interaction model of nitrogen and carbon containing supercells were compared with results obtained from a primitive cell, which only considers the volume-driven effect of interstitial alloying on SFE. In both cases SFE changes from negative to positive upon interstitial alloying, but with significantly different slopes. In the following subsections, the physical basis of the two approaches is discussed and an attempt is made to reconcile the computed SFE values with experimentally determined SFE values and experimentally observed deformation-induced phase transformations.

4.1. Interstitial distribution at the stacking fault

As a comparison and “baseline” for the supercell SFE calculations, SFE calculations at the atomic volumes of the supercells were performed without considering explicit interstitial alloying. Using primitive cells, these calculations were easy to implement and efficient to perform, however, the obtained SFE values from supercell and primitive cell approaches deviate significantly. Only considering the volume-driven effect of interstitials on SFE in the paramagnetic systems, the slope of SFE vs. interstitial occupancy was reduced ~3-fold (Fig. 3 and Fig. 5), whereas in the case of no magnetic interaction this reduction was even more than 13-fold (Fig. 2).

The difference in SFE between these approaches describes two fundamentally different scenarios of the interaction of interstitial atoms with a stacking fault. To visualize this, the *fcc* lattice with interstitial alloying on octahedral sites is depicted in Fig. 8(a). Application of the

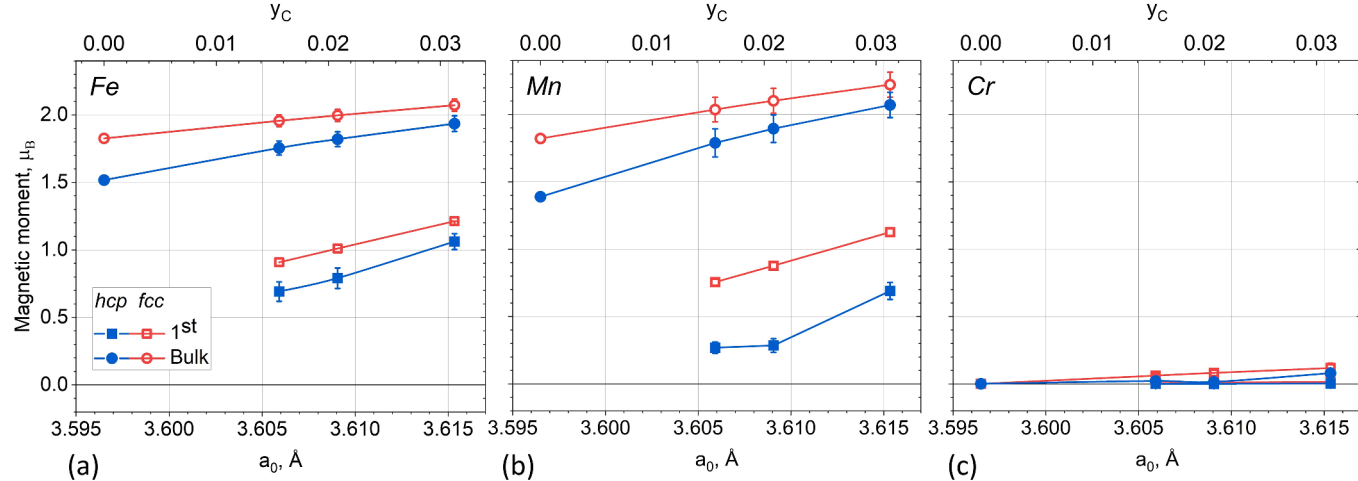


Fig. 6. Magnetic moments of (a) Fe, (b) Mn and (c) Cr in carbon alloyed *fcc* and *hcp* AISI 304 supercells plotted vs. volume and carbon content. Data compares the mean magnetic moment of the six atoms in the 1st coordination shell of the carbon atom (Fig. 1) with the magnetic moment of the remaining bulk atoms. The error bars indicate the standard deviation of the magnetic moments of the considered groups of atoms.

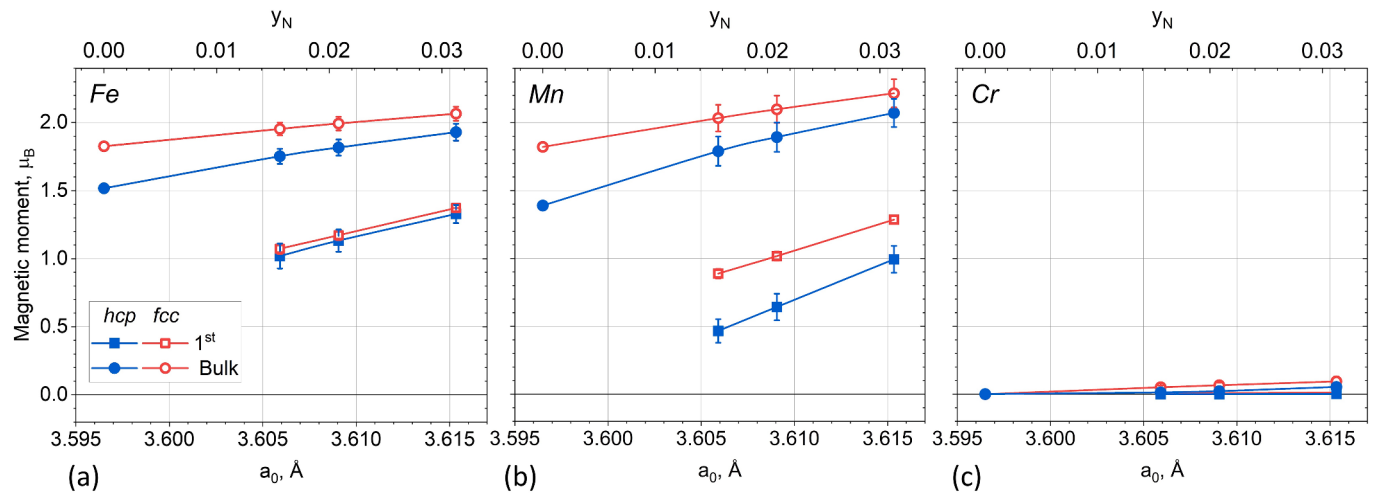


Fig. 7. Magnetic moments of (a) Fe, (b) Mn and (c) Cr in nitrogen alloyed fcc and hcp AISI 304 supercells plotted vs. volume and nitrogen content. Data compares the mean magnetic moment of the six atoms in the 1st coordination shell of the nitrogen atom (Fig. 1) with the magnetic moment of the remaining bulk atoms. The error bars indicate the standard deviation of the magnetic moments of the considered groups of atoms.

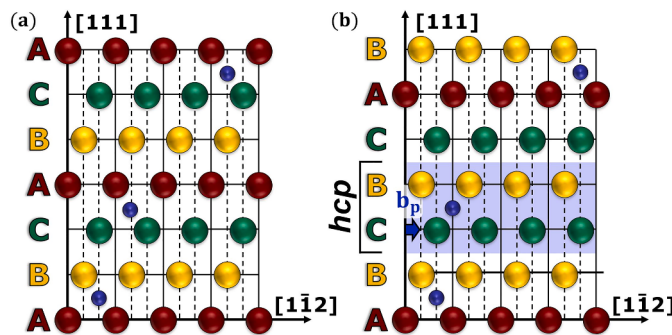


Fig. 8. (a) fcc structure revealing ABC stacking of the {111} planes and containing three interstitial atoms (blue) on octahedral sites. (b) Application of the lattice shear $b_p = \frac{1}{6}[11\bar{2}]$ introduces a stacking fault, which leads to the formation of a local double-layer hcp nucleus. The interstitial concentration in the depicted case is equal in fcc and hcp which is reflected by the supercell approach in this work.

lattice shear introduced by a Shockley partial dislocation, i.e. $b_p = \frac{1}{6}[11\bar{2}]$, leads to the removal of a single A layer and thus to the formation of an intrinsic stacking fault (Fig. 8(b)). Locally, the stacking fault forms an hcp double-layer. In the depicted scenario, the interstitial content is equally shared between the fcc and hcp phases. This scenario is equivalent to applying Eq. (1) to the supercells depicted in Fig. 1. Accordingly, matrix and stacking fault experience the same chemical effect of interstitial alloying. In contrast, modeling the fcc and hcp phases according to their respective primitive cells, where only the average volume change induced by interstitial alloying is accounted for, the chemical effect of interstitial alloying on matrix and stacking fault is omitted. The two methods therefore describe different scenarios of the local carbon and nitrogen distribution at the stacking fault.

The distribution of carbon and nitrogen at the stacking fault is challenging to characterize experimentally and its nature is therefore unclear. Using in-situ transmission electron microscopy, Hickel et al. [96] observed widening of stacking faults during heating, associated with a decrease in measured SFE. Backed with results from computational thermodynamics, the authors interpreted the widening of the stacking fault to be induced by diffusion of carbon away from the stacking fault. The observation suggests that, given thermal activation, the carbon content within the stacking fault could be lower than the value in the bulk. In general, it is however unlikely for carbon and

nitrogen to diffuse away from the stacking fault under ambient conditions, which gives some merit to the scenario of a homogeneous distribution of interstitials within the bulk and stacking fault, as represented by the supercell approach.

Another mechanism that is characteristic for interstitials, is their tendency to strongly interact with partial dislocations [97], for example by pinning partials via the formation of solute-C/N pairs (short range ordering) through the fast diffusion along dislocation cores [98], even at or below room temperature. Therefore, the observed SF width in experiments will be strongly affected by partial-interstitial interaction and measuring the stacking fault width will likely not reflect the effect of interstitials on the SFE [96,97,99].

4.2. Short-range ordering of interstitial atoms with Cr

The SFE values computed for the AISI 304 composition as a function of interstitial content rely on the assumption that the interstitial atoms experience the chemical effect of the mean substitutional alloy composition in their immediate surrounding. It is however known that carbon,

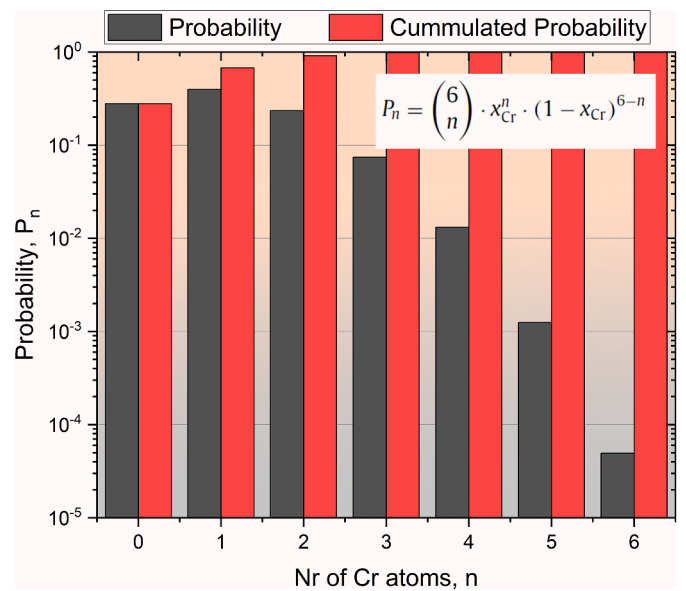


Fig. 9. Probabilities of encountering n Cr atoms around an octahedrally coordinated interstice for the AISI 304 composition (19.14 at.% Cr).

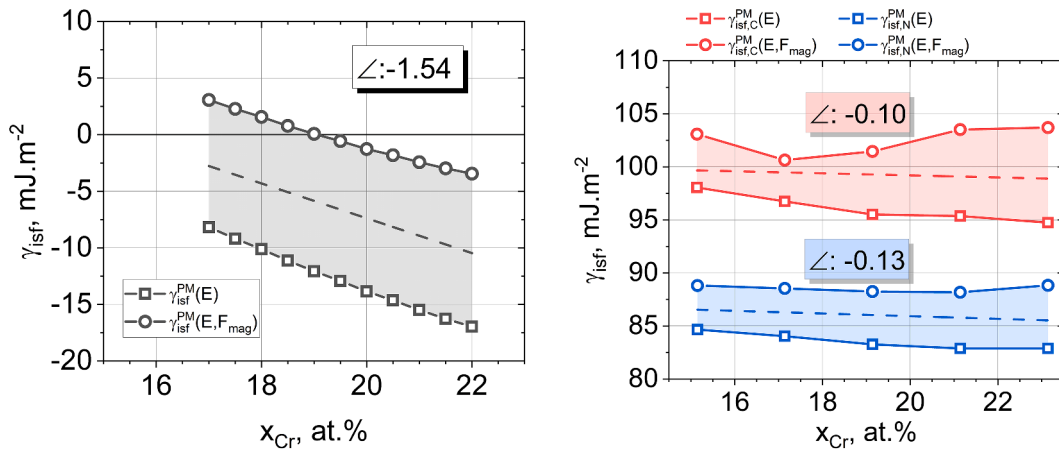


Fig. 10. Effect of Cr content on the SFE of (a) interstitial-free AISI 304 (condition $y = 0$ in Fig. 5) and (b) AISI 304 with $y = 0.0313$ for C (red) and N (blue).

and particularly nitrogen, preferentially attempt to occupy interstices surrounded by as many Cr atoms as possible [100]. Assuming a random distribution of Cr atoms within the fcc lattice, Fig. 9 shows the probability that the octahedrally coordinated interstices are surrounded by 0 to 6 Cr atoms [101].

Considering that all interstitial atoms preferentially occupy the interstices with most Cr neighbors first, the maximum considered interstitial occupancy of $y=0.0313$ in this work would lead to the occupation of all interstices surrounded by 6, 5 and 4 Cr atoms as well as 23% of the interstices with 3 Cr atoms. While this scenario describes an extreme case, it is plausible that for very low interstitial contents Cr would partially shield Fe atoms from direct interaction with the interstitials. It however remains unclear to which extent the formation of a stacking fault, a large planar defect, is dominated by the kinetics and thermodynamics at the local vs. the global microstructure scale [4, 102].

Ab initio techniques have limitations that inhibit a detailed study on the effect of short range ordering on SFE values for the paramagnetic interstitial alloy AISI 304. A detailed study would require the divergence from the here employed CPA model to enable explicit modeling of the local site occupation of the substitutional lattice surrounding the interstices. Realistic total energies for such configurations would require a more complex ionic relaxation which cannot be employed with the current EMTO formalism. Other ab initio formalisms than EMTO would not be able to appropriately consider the effect of the paramagnetic state.

Some indication on the effect of C and N short range ordering with Cr on the SFE can be obtained from analyzing the effect of a deviating Cr content on the SFE values in AISI 304 in the interstitial-free condition (Fig. 10(a)) and the maximum interstitial occupation of $y=0.0313$ (Fig. 10(b)). In the interstitial-free condition the SFE reduces with ~ 1.5 mJ·m⁻² per at.% Cr. Considering that short-range ordering “traps” some Cr atoms by C and/or N, the reduced Cr content in the interstitial-free regions would, similar to the C- and N-rich regions, lead to an increase in SFE. Considering an interstitial occupancy of $y=0.0313$, the effect of a variation in Cr content on SFE is greatly reduced. It appears that the overall chemical effect of C and N alloying overshadows the effect of moderate changes in the substitutional composition. A more detailed treatment of the effect of short range ordering of C and N in Cr-alloyed steels is an important perspective for future research.

4.3. Interstitially-induced negative-to-positive SFE transition in AISI 304

Considering the mean value of the SFE values $\gamma_{\text{isf,C/N}}^{\text{PM}}(E)$ and $\gamma_{\text{isf,C/N}}^{\text{PM}}(E, F_{\text{mag}})$, the ab initio methods show a transition from negative to positive SFE with increasing interstitial content for AISI 304. Fig. 5 shows that the SFE in AISI 304 changes from a negative to a positive value at a

nitrogen occupancy of 0.0016 ($\cong 0.04$ wt%N) when considering the volume-chemistry-driven effect and at 0.0037 ($= 0.094$ wt%N) when considering only the volume-driven effect on SFE. These values are interpreted as the critical nitrogen contents above which thermodynamical stability is reached. These results are compared to experimentally observed transformation behavior in metastable alloys. Wang et al. [95] applied severe mechanical deformation to AISI 304L that contains a variation in nitrogen content from 0.4 wt% N at the surface to 0.024 wt % N in the core. It is well established that AISI 304 is metastable and may form ε -martensite and α' -martensite upon mechanical loading [103–106]. It was found that nitrogen contents > 0.1 wt% N suppressed martensite formation for cold rolling up to 50% strain, while higher degrees of deformation (up to 70%) required 0.3 wt% N to prevent martensite formation (see Fig. 11). Instead, deformation twinning and dislocation slip established plastic deformation [87]. Apparently, nitrogen alloying stabilizes austenite which is consistent with an increase in SFE. The critical nitrogen content of about 0.1 wt% N for suppression of martensite formation up to 50% cold rolling compares favourably with the negative-to-positive transition given by the volume-driven effect at 0.094 wt% N (Fig. 5). This observation supports the understanding that for low interstitial content the SFE evolution with interstitial content will be partly volume-driven, as nitrogen is trapped at Cr-coordinated interstices (see Section 4.2). Due to the complexity involved in stacking fault formation in interstitially alloyed steels outlined in Section 4.1, this experimental observation is insufficient to quantitatively validate the ab initio approach or vice versa, but it

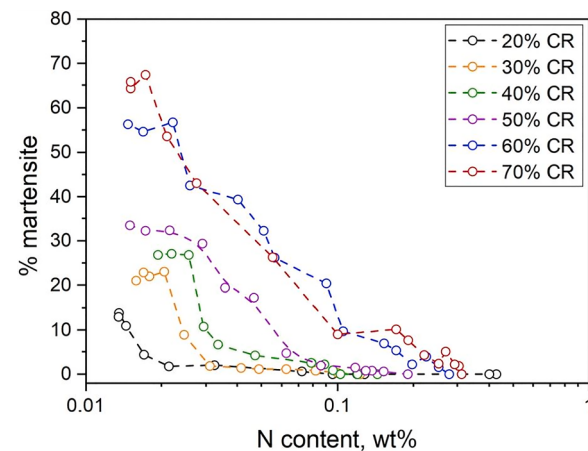


Fig. 11. Fraction of martensite as a function of nitrogen content and cold-rolling (CR) reduction. Reproduced from Ref. [95] with permission from Springer Nature.

demonstrates that the general picture between transformation behavior and SFE thermodynamics is consistent.

4.4. Validation with experimentally determined SFE values

Table 3 gives an overview of experimentally determined SFE values from literature for different compositions close to the one of AISI 304. The average value from 18 data points is $\gamma_{isf}^{Exp} = 20.8 \text{ mJ.m}^{-2}$. The average carbon and nitrogen occupancies of the alloys in **Table 3** are 0.00196 (=0.043 wt% C) and 0.00125 (=0.032 wt% N), respectively. Analysis of the data in **Table 3** shows no clear trend between the SFE values and the interstitial contents. Evidently, different measurement methods, different heat treatment conditions and variation in substitutional alloy composition introduce so much variation in SFE, that the effect of interstitials is obscured. In this respect a clear trend is observed between SFE and the Ni content (**Fig. 12**: positive values in red). The observed trend of SFE vs. Ni content from literature is in reasonable agreement with the predicted trend from DFT (**Fig. 10**: negative values in blue). The y-intercepts of the slopes of straight lines fitted with linear regression through experimental and predicted values are offset by -12 mJ.m^{-2} .

As discussed in **Section 1**, for metastable alloys SFE values obtained with DFT cannot be compared directly with experimental SFE values [10]. Werner et al. [8] developed an approach that reconciles experimental and theoretical SFE values by reconsidering the incomplete force balance acting on the Shockley partials. The apparent SFE value determined from experiment, γ_{isf}^{Exp} , and the actual SFE value, γ_{isf} , which, within computational error, corresponds to the value from ab initio calculations, are related by [8]:

$$\gamma_{isf} = \gamma_{isf}^{Exp} - b_p \left(\tau_{0,twin} + \frac{K_{twin}^{HP}}{\sqrt{D}} \right) \quad (6)$$

where b_p is the Burgers vector of the partial dislocation, D is the grain size, $\tau_{0,twin}$ is the critical resolved shear stress for twinning of a single crystalline material due to lattice friction and solid solution hardening, and K_{twin}^{HP} is the critical resolved shear stress' Hall-Petch slope. The discrepancy between computationally and experimentally determined SFE values is thereby attributed to $b_p (\tau_{0,twin} + \frac{K_{twin}^{HP}}{\sqrt{D}})$, where, provided that the grain size is not too small, $b_p \tau_{0,twin}$ is the dominant contribution that introduces the offset. Applying **Eq. (6)**, a convincing quantitative

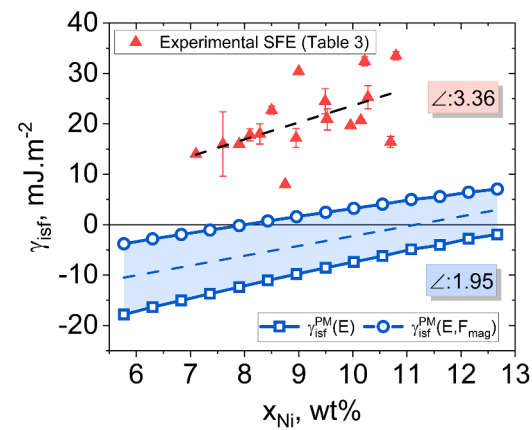


Fig. 12. Effect of Ni content on the ab initio SFE of interstitial-free AISI 304 compared with the effect of Ni on the experimental SFE in AISI 304 alloys from literature (**Table 2**). The ab initio SFE increases 1.95 mJ.m^{-2} per wt% Ni. Despite large scatter in the literature data, the fitted slope of 3.36 mJ.m^{-2} per wt% Ni is in reasonable agreement with the DFT results.

agreement was found for both stable and metastable fcc metals, including pure metals and medium-/high-entropy alloys [8,9].

Using **Eq. (6)** for AISI 304, we adopt $\tau_{0,twin} = 262 \text{ MPa}$ for an AISI 304 austenitic stainless steel by Talonen et al. [103]; this (experimental) value is derived from the mean applied stress at which ϵ -martensite formation is observed and a maximum Schmid factor of 0.5. Taking $b_p = a_{fcc}/\sqrt{6}$ with $a_{fcc} = 3.598 \text{ \AA}$ for an overall interstitial occupancy of 0.00321 [82], the actual SFE value becomes -18 mJ.m^{-2} .

This value of -18 mJ.m^{-2} is somewhat lower than the calculated SFE values for 8.1 wt% Ni in Ref. [103], which range from -12 to 0 mJ.m^{-2} . The offset between γ_{isf}^{Exp} and γ_{isf}^{PM} is likely caused by the forces affecting the kinetics of stacking fault formation. The effect of Ni on the SFE is generally not universal, as assumed here, but depends strongly on the host alloy composition [36–38]. Unfortunately, no systematic experimental study of the effect of nitrogen content on the SFE in AISI 304 with constant metallic composition is available; only data for different austenitic steels is available [50,58,60,62]. More systematic experimental and computational efforts are therefore required to cement this relationship for important austenitic alloy grades.

Table 3

Experimental SFE values, γ_{isf}^{Exp} , in mJ.m^{-2} of AISI 304 sorted by ascending Cr content. All compositions are in wt% and substitutional alloying elements contributing < 0.2 wt% were discarded.

Ref.	Fe	Cr	Ni	Mn	Mo	Si	Cu	C	N	γ_{isf}^{Exp}
Butakova et al. 1972 [107]	74.86	17.50	7.60	–	–	–	–	0.040	–	16 ± 6.4
Swann*, 1963 [61]	74.40	17.60	7.90	–	–	–	–	0.060	0.040	16
Fussik et al., 2021 [108]	70.22	17.70	8.50	1.90	0.30	0.70	0.60	0.026	0.053	22.7 ± 0.8
Swann*, 1963 [61]	74.83	17.90	7.10	–	–	–	–	0.060	0.110	14
Borges et al., 1985 [109]	70.69	18.11	9.49	0.91	0.33	0.41	–	0.057	–	24.5 ± 2.5
Yang & Spruiell, 1982 [110]	71.33	18.20	8.75	1.36	–	0.32	–	0.040	0.005	8
Pontini & Hermida, 1997 [111]	70.92	18.20	9.00	1.20	0.20	0.40	–	0.042	0.040	30.4
Talonen & Hänninen, 2007 [103]	71.90	18.20	8.10	1.71	–	–	–	0.041	0.054	17.8 ± 1.2
Latanision & Ruff, 1971 [112]	71.00	18.30	10.70	–	–	–	–	0.005	–	16.4 ± 1.1
Dulieu & Nutting*, 1964 [48]	70.38	18.30	10.28	0.64	–	0.30	–	0.079	0.020	25.3 ± 2.3
Schramm & Reed, 1975 [44]	72.25	18.31	8.28	0.82	–	0.30	–	0.025	0.018	18 ± 2
Borges et al., 1985 [109]	67.95	18.35	9.53	0.83	2.10	1.17	–	0.071	–	20.9 ± 2.1
Murr, 1969 [113]	71.07	18.43	9.52	0.50	–	0.42	–	0.058	–	21
Dulieu & Nutting*, 1964 [48]	70.03	18.45	10.15	0.66	–	0.43	–	0.079	0.200	20.7
Yonezawa et al., 2013 [114]	69.58	18.56	10.22	1.03	–	0.57	–	0.020	0.020	32.4 ± 0.86
Borges et al., 1985 [109]	70.37	18.60	8.95	0.82	0.32	0.88	–	0.063	–	17.2 ± 1.9
Yonezawa et al., 2013 [114]	69.03	19.00	10.80	0.85	0.30	–	–	0.016	0.008	33.5 ± 0.8
Kaneko, 1996 [115]	70.91	19.13	9.96	–	–	–	–	<0.01	–	19.7
										Mean: 20.8

* The reported value was multiplied by 2.3 [116,117].

† Corrected using elastic constants from Ref. [44].

5. Conclusion

This work featured the calculation of the intrinsic stacking-fault energy (SFE) as a function of interstitial nitrogen and carbon contents in non-magnetic and paramagnetic γ -Fe, as well as in paramagnetic AISI 304 austenitic stainless steels, using ab initio thermodynamics. The conclusions can be summarized as follows:

- 1) In all considered systems, the SFE increased approximately linearly with the occupancy of the interstitial lattice. The initial values for the SFE in the interstitial-free condition and the slopes with increasing interstitial occupancy differed significantly among the considered systems.
- 2) Including the paramagnetic state using the disordered localized moments model increased the SFE values by $\sim 385 \text{ mJ.m}^{-2}$. It is thus crucial to include the proper magnetic contribution when modeling SFE in austenitic stainless steels.
- 3) Paramagnetic γ -Fe and AISI 304 underwent a metastable-to-stable transition at interstitial occupancies of 0.0011 ($\sim 0.028 \text{ wt\%}$) and 0.0016 ($\sim 0.04 \text{ wt\%}$), respectively.
- 4) At low interstitial content, interstitials may be trapped in Cr-surrounded octahedral interstices that could partly promote a volume-driven effect of interstitial alloying on SFE. Considering this effect, good agreement could be obtained with the critical nitrogen content that suppresses strain-induced martensite formation in an experimental study.
- 5) Applying the method by Werner et al. [8], ab initio SFE values for AISI 304 were reconciled with an error of 6 - 18 mJ.m^{-2} . The correction method includes an, as of now, unaccounted contribution in experimental SFE determination.
- 6) The SFE of AISI 304 was calculated to increase with 1.95 mJ.m^{-2} per wt% Ni, which is in fair agreement with experimental data.

Declaration of Competing Interest

The authors declare that they have no known competing financial interests or personal relationships that could have appeared to influence the work reported in this paper.

Acknowledgments

This work was supported by the Independent Research Fund Denmark as part of the project SFETailor (Grant No. 9041-00145B). The computation was performed using the Niflheim cluster at the Technical University of Denmark. S. Lu thanks the support within the project "SuperFraMat" by Vinnova and the Strategic Mobility grant by the Swedish Foundation for Strategic Research (SSF). L. Vitos acknowledges the Swedish Research Council (VR), SSF, VINNOVA, the Swedish Foundation for International Cooperation in Research and Higher Education (STINT), the Hungarian Scientific Research Fund (OTKA 128229), and the Carl Tryggers Foundation for financial support.

References

- [1] B.C. De Cooman, Y. Estrin, S.K. Kim, Twinning-induced plasticity (TWIP) steels, *Acta Mater.* 142 (2018) 283–362, <https://doi.org/10.1016/j.actamat.2017.06.046>.
- [2] Z. Li, F. Körmann, B. Grabowski, J. Neugebauer, D. Raabe, Ab initio assisted design of quinary dual-phase high-entropy alloys with transformation-induced plasticity, *Acta Mater.* 136 (2017) 262–270, <https://doi.org/10.1016/j.actamat.2017.07.023>.
- [3] O. Güvenç, F. Roters, T. Hickel, M. Bambach, ICME for crashworthiness of TWIP Steels: from ab initio to the crash performance, *JOM* 67 (2015) 120–128, <https://doi.org/10.1007/s11837-014-1192-8>.
- [4] J. Ding, Q. Yu, M. Asta, R.O. Ritchie, Tunable stacking fault energies by tailoring local chemical order in CrCoNi medium-entropy alloys, *Proc. Natl. Acad. Sci. U. S. A.* 115 (2018) 8919–8924, <https://doi.org/10.1073/pnas.1808660115>.
- [5] T.Z. Khan, T. Kirk, G. Vazquez, P. Singh, A.V. Smirnov, D.D. Johnson, K. Youssef, R. Arróyave, Towards stacking fault energy engineering in FCC high entropy alloys, *Acta Mater.* 224 (2022) 117472, <https://doi.org/10.1016/j.actamat.2021.117472>.
- [6] T. Hickel, A. Dick, B. Grabowski, F. Körmann, J. Neugebauer, Steel design from fully parameter-free ab initio computer simulations, *Steel Res. Int.* 80 (2009) 4–8, <https://doi.org/10.2374/SRI08SP109>.
- [7] Z. Li, K.G. Pradeep, Y. Deng, D. Raabe, C.C. Tasan, Metastable high-entropy dual-phase alloys overcome the strength-ductility trade-off, *Nature* 534 (2016) 227–230, <https://doi.org/10.1038/nature17981>.
- [8] K.V. Werner, F. Niessen, M. Villa, M.A.J. Somers, Experimental validation of negative stacking fault energies in metastable face-centered cubic materials, *Appl. Phys. Lett.* 119 (2021), <https://doi.org/10.1063/5.0063761>.
- [9] K.V. Werner, F. Niessen, W. Li, S. Lu, L. Vitos, M. Villa, M.A.J. Somers, Reconciling experimental and theoretical stacking fault energies in face-centered cubic materials with the experimental twinning stress, *Materialia* 27 (2023) 101708, <https://doi.org/10.1016/j.matla.2023.101708>. ISSN 2589-1529.
- [10] X. Sun, S. Lu, R. Xie, X. An, W. Li, T. Zhang, C. Liang, X. Ding, Y. Wang, H. Zhang, L. Vitos, Can experiment determine the stacking fault energy of metastable alloys? *Mater. Des.* 199 (2021), 109396 <https://doi.org/10.1016/j.matdes.2020.109396>.
- [11] M. Shih, J. Miao, M. Mills, M. Ghazisaeidi, Stacking fault energy in concentrated alloys, *Nat. Commun.* 12 (2021) 1–10, <https://doi.org/10.1038/s41467-021-23860-z>.
- [12] Y.K. Lee, C. Choi, Driving force for $\gamma \rightarrow \epsilon$ martensitic transformation and stacking fault energy of γ in Fe-Mn binary system, *Metall. Mater. Trans. A* 31 (2000) 355–360, <https://doi.org/10.1007/s11661-000-0271-3>.
- [13] S.M. Lee, S.J. Lee, S. Lee, J.H. Nam, Y.K. Lee, Tensile properties and deformation mode of Si-added Fe-18Mn-0.6C steels, *Acta Mater.* 144 (2018) 738–747, <https://doi.org/10.1016/j.actamat.2017.11.023>.
- [14] J. Chen, F.T. Dong, Z.Y. Liu, G.D. Wang, Grain size dependence of twinning behaviors and resultant cryogenic impact toughness in high manganese austenitic steel, *J. Mater. Res. Technol.* 10 (2021) 175–187, <https://doi.org/10.1016/j.jmrt.2020.12.030>.
- [15] S.J. Lee, K. Ushioda, H. Fujii, Evaluation of stacking-fault energy in Fe-Mn based twinning-induced plasticity steels after friction stir welding, *Mater. Charact.* 147 (2019) 379–383, <https://doi.org/10.1016/j.matchar.2018.11.024>.
- [16] S. Wei, C.C. Tasan, Deformation faulting in a metastable CoCrNiW complex concentrated alloy: a case of negative intrinsic stacking fault energy? *Acta Mater.* 200 (2020) 992–1007, <https://doi.org/10.1016/j.actamat.2020.09.056>.
- [17] U.R. Kattner, The thermodynamic modeling of multicomponent phase equilibria, *JOM* 49 (1997) 14–19, <https://doi.org/10.1007/s11837-997-0024-5>.
- [18] P. Hohenberg, W. Kohn, Inhomogeneous Electron Gas, *Phys. Rev.* 136 (1964) 864–871, <https://doi.org/10.1007/BF01198136>.
- [19] W. Kohn, L.J. Sham, Self-Consistent Equations Including Exchange and Correlation Effects, *Phys. Rev.* 140 (1965) 1133–1138.
- [20] A. Saeed-Akbari, J. Imlau, U. Prahl, W. Bleck, Derivation and variation in composition-dependent stacking fault energy maps based on subregular solution model in high-manganese steels, *Metall. Mater. Trans. A Phys. Metall. Mater. Sci.* 40 (2009) 3076–3090, <https://doi.org/10.1007/s11661-009-0050-8>.
- [21] S. Allain, J.P. Chateau, O. Bouaziz, S. Migot, N. Guelton, Correlations between the calculated stacking fault energy and the plasticity mechanisms in Fe-Mn-C alloys, *Mater. Sci. Eng. A* 387–389 (2004) 158–162, <https://doi.org/10.1016/j.msea.2004.01.059>.
- [22] O.A. Zambrano, Stacking fault energy maps of Fe-Mn-Al-C-Si steels: effect of temperature, grain size, and variations in compositions, *J. Eng. Mater. Technol., Trans. ASME.* 138 (2016), <https://doi.org/10.1115/1.4033632>.
- [23] D.T. Pierce, J.A. Jiménez, J. Bentley, D. Raabe, C. Oskay, J.E. Wittig, The influence of manganese content on the stacking fault and austenite/e-martensite interfacial energies in Fe-Mn-(Al-Si) steels investigated by experiment and theory, *Acta Mater.* 68 (2014) 238–253, <https://doi.org/10.1016/j.actamat.2014.01.001>.
- [24] O. Gräßel, G. Frommeyer, C. Derder, H. Hofmann, Phase transformations and mechanical properties of Fe-Mn-Si-Al TRIP-steels phase transformations and mechanical properties of Fe-Mn-Si-Al TRIP-steels, *J. Phys. IV Proc.* 7 (1997) 7, <https://doi.org/10.1051/jp4:1997560>.
- [25] G.B. Olson, M. Cohen, A general mechanism of martensitic nucleation: part I. General concepts and the FCC /HCP transformation, *Metall. Trans. A* 7 (1976) 1897–1904, <https://doi.org/10.1007/BF02659822>.
- [26] S. Curtze, V.T. Kuokkala, A. Oikari, J. Talonen, H. Hänninen, Thermodynamic modeling of the stacking fault energy of austenitic steels, *Acta Mater.* 59 (2011) 1068–1076, <https://doi.org/10.1016/j.actamat.2010.10.037>.
- [27] R. Li, S. Lu, D. Kim, S. Schönecker, J. Zhao, S.K. Kwon, L. Vitos, Stacking fault energy of face-centered cubic metals: thermodynamic and ab initio approaches, *J. Phys. Condens. Matter* 28 (2016), <https://doi.org/10.1088/0953-8984/28/39/395001>.
- [28] S. Bigdeli, H. Ehtehami, Q. Chen, H. Mao, P. Korzhavy, M. Selleby, New description of metastable hcp phase for unaries Fe and Mn: coupling between first-principles calculations and CALPHAD modeling, *Phys. Status Solidi B Basic Res.* 253 (2016) 1830–1836, <https://doi.org/10.1002/pssb.201600096>.
- [29] S. Bigdeli, M. Selleby, A thermodynamic assessment of the binary Fe-Mn system for the third generation of Calphad databases, *Calphad* 64 (2019) 185–195, <https://doi.org/10.1016/j.calphad.2018.11.011>.
- [30] P.J.H. Denteneer, W. Van Haeringen, Stacking-fault energies in semiconductors from first-principles calculations, *J. Phys. C Solid State Phys.* 20 (1987) L883–L887, <https://doi.org/10.1088/0022-3719/20/32/001>.

- [31] C. Cheng, R.J. Needs, V. Heine, Inter-layer interactions and the origin of sic polytypes, *J. Phys. C Solid State Phys.* 21 (1988) 1049–1063, <https://doi.org/10.1088/0022-3719/21/6/012>.
- [32] M. Jahnátek, J. Hafner, M. Krajčí, Shear deformation, ideal strength, and stacking fault formation of fcc metals: a density-functional study of Al and Cu, *Phys. Rev. B Condens. Matter Mater. Phys.* 79 (2009), <https://doi.org/10.1103/PhysRevB.79.224103>.
- [33] Y. Wang, M. Liao, B.J. Bocklund, P. Gao, S.L. Shang, H. Kim, A.M. Beese, L.Q. Chen, Z.K. Liu, DFTTK: density functional theory ToolKit for high-throughput lattice dynamics calculations, *Calphad* 75 (2021), 102355, <https://doi.org/10.1016/j.calphad.2021.102355>.
- [34] X. Zhang, B. Grabowski, F. Körmann, A.V. Ruban, Y. Gong, R.C. Reed, T. Hickel, J. Neugebauer, Temperature dependence of the stacking-fault Gibbs energy for Al, Cu, and Ni, *Phys. Rev. B* 98 (2018), <https://doi.org/10.1103/PhysRevB.98.224106>.
- [35] N.D. Mermin, Thermal properties of the inhomogeneous electron gas, *Phys. Rev.* 137 (1965) 1–3, <https://doi.org/10.1103/PhysRev.137.A1441>.
- [36] L. Vitos, J.O. Nilsson, B. Johansson, Alloying effects on the stacking fault energy in austenitic stainless steels from first-principles theory, *Acta Mater.* 54 (2006) 3821–3826, <https://doi.org/10.1016/j.actamat.2006.04.013>.
- [37] L. Vitos, P.A. Korzhavyi, J.O. Nilsson, B. Johansson, Stacking fault energy and magnetism in austenitic stainless steels, *Phys. Scr.* 77 (2008) 12–15, <https://doi.org/10.1088/0031-8949/77/06/065703>.
- [38] J. Lu, L. Hultman, E. Holmström, K.H. Antonsson, M. Grehk, W. Li, L. Vitos, A. Golpayegani, Stacking fault energies in austenitic stainless steels, *Acta Mater.* 111 (2016) 39–46, <https://doi.org/10.1016/j.actamat.2016.03.042>.
- [39] N.I. Medvedeva, M.S. Park, D.C. Van Aken, J.E. Medvedeva, First-principles study of Mn, Al and C distribution and their effect on stacking fault energies in fcc Fe, *J. Alloys Compd.* 582 (2014) 475–482, <https://doi.org/10.1016/j.jallcom.2013.08.089>.
- [40] A. Dick, T. Hickel, J. Neugebauer, The effect of disorder on the concentration-dependence of stacking fault energies in Fe 1-x Mn x – a first principles study, *Steel Res. Int.* 80 (2009) 603–608, <https://doi.org/10.2374/SRI09SP015>.
- [41] Y.W. Choi, Z. Dong, W. Li, S. Schönecker, H. Kim, S.K. Kwon, L. Vitos, Predicting the stacking fault energy of austenitic Fe-Mn-Al (Si) alloys, *Mater. Des.* 187 (2020), 108392, <https://doi.org/10.1016/j.matdes.2019.108392>.
- [42] Z. Dong, S. Schönecker, D. Chen, W. Li, S. Lu, L. Vitos, Influence of Mn content on the intrinsic energy barriers of paramagnetic FeMn alloys from longitudinal spin fluctuation theory, *Int. J. Plast.* 119 (2019) 123–139, <https://doi.org/10.1016/j.ijplas.2019.02.020>.
- [43] L. Norström, The influence of nitrogen and grain size on yield strength in type AISI 316L austenitic stainless steel, *Met. Sci.* 11 (1977) 208–212, <https://doi.org/10.1179/msc.1977.11.6.208>.
- [44] R.E. Schramm, R.P. Reed, Stacking fault energies of seven commercial austenitic stainless steels, *Metall. Trans. A* 6A (1975) 1345–1351.
- [45] J. Singh, Influence of deformation on the transformation of austenitic stainless steels, *J. Mater. Sci.* 20 (1985) 3157–3166, <https://doi.org/10.1007/BF00545181>.
- [46] J. Nakano, A thermo-mechanical correlation with driving forces for hcp martensite and twin formations in the Fe-Mn-C system exhibiting multicomposition sets, *Sci. Technol. Adv. Mater.* 14 (2013), <https://doi.org/10.1088/1468-6996/14/1/014207>.
- [47] T.H. Lee, H.Y. Ha, B. Hwang, S.J. Kim, E. Shin, Effect of carbon fraction on stacking fault energy of austenitic stainless steels, *Metall. Mater. Trans. A Phys. Metall. Mater. Sci.* 43 (2012) 4455–4459, <https://doi.org/10.1007/s11661-012-1423-y>.
- [48] D. Dulieu, J. Nutting, *Influence of Solute Additions On the Stacking Fault Energy of Iron-Nickel-Chromium austenites*, London, 1964.
- [49] P.Y. Vološevič, V.N. Gridnev, Y.N. Petrov, Influence of carbon on the stacking fault energy of austenite in manganese steels, *Phys. Met. Metallogr.* 40 (1975) 90–94.
- [50] N. Saenarjhan, J.H. Kang, S.J. Kim, Effects of carbon and nitrogen on austenite stability and tensile deformation behavior of 15Cr-15Mn-4Ni based austenitic stainless steels, *Mater. Sci. Eng. A* 742 (2019) 608–616, <https://doi.org/10.1016/j.msea.2018.11.048>.
- [51] P.R. Swann, Dislocation Substructure vs Transgranular Stress Corrosion Susceptibility Of Single Phase Alloys, *Corrosion* 3 (1963) 102–114.
- [52] R. Fawley, M.A. Quader, R.A. Dodd, Compositional effects on the deformation modes, annealing twin frequencies, and stacking fault energies of austenitic stainless steels, *Trans. Metall. Soc. AIME* 242 (1968) 771–776.
- [53] R.E. Stoltz, J.B. van der Sande, The effect of nitrogen on stacking fault energy of Fe-Ni-Cr-Mn steels, *Metall. Trans. A* 11A (1980) 1033–1037.
- [54] W. Charnock, J. Nutting, The effect of carbon and nickel upon the stacking-fault energy of iron, *Met. Sci. J.* 1 (1967) 123–127.
- [55] Y.U.N. Petrov, Effect of carbon and nitrogen on the stacking fault energy of high-alloyed iron-based austenite, *Int. J. Mater. Res.* 94 (2003) 1012.
- [56] L. Bracke, G. Mertens, J. Penning, B.C. De Cooman, M. Liebeherr, N. Akdut, Influence of phase transformations on the mechanical properties of high-strength austenitic Fe-Mn-Cr steel, *Metall. Mater. Trans. A Phys. Metall. Mater. Sci.* 37 (2006) 307–317, <https://doi.org/10.1007/s11661-006-0002-5>.
- [57] B.X. Huang, X.D. Wang, L. Wang, Y.H. Rong, Effect of nitrogen on stacking fault formation probability and mechanical properties of twinning-induced plasticity steels, *Metall. Mater. Trans. A Phys. Metall. Mater. Sci.* 39 A (2008) 717–724, <https://doi.org/10.1007/s11661-007-9434-9>.
- [58] S.J. Lee, Y.S. Jung, S. Il Baik, Y.W. Kim, M. Kang, W. Woo, Y.K. Lee, The effect of nitrogen on the stacking fault energy in Fe-15Mn-2Cr-0.6C-xN twinning-induced plasticity steels, *Scr. Mater.* 92 (2014) 23–26, <https://doi.org/10.1016/j.scriptamat.2014.08.004>.
- [59] M. Ojima, Y. Adachi, Y. Tomota, Y. Katada, Y. Kaneko, K. Kuroda, H. Saka, Weak beam TEM study on stacking fault energy of high nitrogen steels, *Steel Res. Int.* 80 (2009) 477–481, <https://doi.org/10.2374/SRI09SP038>.
- [60] T.H. Lee, E. Shin, C.S. Oh, H.Y. Ha, S.J. Kim, Correlation between stacking fault energy and deformation microstructure in high-interstitial-alloyed austenitic steels, *Acta Mater.* 58 (2010) 3173–3186, <https://doi.org/10.1016/j.actamat.2010.01.056>.
- [61] P.R. Swann, Dislocation substructure vs. transgranular stress corrosion susceptibility of single phase alloys, *Corrosion* 19 (1963) 102–112.
- [62] Y. Kawahara, R. Teranishi, C. Takushima, J.I. Hamada, K. Kaneko, Effect of nitrogen addition on the stacking-fault energies in Si-added austenitic stainless steel, *ISIJ Int.* 61 (2021) 1029–1036, <https://doi.org/10.2355/ISIJINTERNATIONAL.ISIJINT-2020-609>.
- [63] M. Fujikura, K. Takada, K. Ishida, Effect of manganese and nitrogen on the mechanical properties of Fe-18%Cr-10%Ni stainless steels, *Trans. Iron Steel Inst. Jap.* 15 (1975) 464–469, <https://doi.org/10.2355/isijinternational1966.15.464>.
- [64] S. Wang, K. Yang, Y. Shan, L. Li, Plastic deformation and fracture behaviors of nitrogen-alloyed austenitic stainless steels, *Mater. Sci. Eng. A* 490 (2008) 95–104, <https://doi.org/10.1016/j.msea.2008.01.015>.
- [65] V. Gavriljuk, Y. Petrov, B. Shanina, Effect of nitrogen on the electron structure and stacking fault energy in austenitic steels, *Scr. Mater.* 55 (2006) 537–540, <https://doi.org/10.1016/j.scriptamat.2006.05.025>.
- [66] S. Kibey, J.B. Liu, M.J. Curtis, D.D. Johnson, H. Sehitoglu, Effect of nitrogen on generalized stacking fault energy and stacking fault widths in high nitrogen steels, *Acta Mater.* 54 (2006) 2991–3001, <https://doi.org/10.1016/j.actamat.2006.02.048>.
- [67] H. Gholizadeh, C. Draxl, P. Puschnig, The influence of interstitial carbon on the γ-surface in austenite, *Acta Mater.* 61 (2013) 341–349, <https://doi.org/10.1016/j.actamat.2012.09.066>.
- [68] A. Abbasi, A. Dick, T. Hickel, J. Neugebauer, First-principles investigation of the effect of carbon on the stacking fault energy of Fe-C alloys, *Acta Mater.* 59 (2011) 3041–3048, <https://doi.org/10.1016/j.actamat.2011.01.044>.
- [69] S. Lu, R. Li, K. Kádas, H. Zhang, Y. Tian, S.K. Kwon, K. Kokko, Q.M. Hu, S. Hertzman, L. Vitos, Stacking fault energy of C-alloyed steels: the effect of magnetism, *Acta Mater.* 122 (2017) 72–81, <https://doi.org/10.1016/j.actamat.2016.09.038>.
- [70] L. Vitos, P.A. Korzhavyi, B. Johansson, Evidence of large magnetostructural effects in austenitic stainless steels, *Phys. Rev. Lett.* 96 (2006) 1–4, <https://doi.org/10.1103/PhysRevLett.96.117210>.
- [71] G. Grimvall, Spin disorder in paramagnetic fcc iron, *Phys. Rev. B* 39 (1989) 12300–12301, <https://doi.org/10.1103/PhysRevB.39.12300>.
- [72] S.L. Shang, W.Y. Wang, Y. Wang, Y. Du, J.X. Zhang, A.D. Patel, Z.K. Liu, Temperature-dependent ideal strength and stacking fault energy of fcc Ni: a first-principles study of shear deformation, *J. Phys. Condens. Matter* 24 (2012), <https://doi.org/10.1088/0953-8984/24/15/155402>.
- [73] H. Gholizadeh, The influence of alloying and temperature on the stacking-fault energy of iron-based alloys, *PhD Dissert.* Montanuniv. Leoben (2013) 193.
- [74] A.V. Ruban, S. Khmelevskyi, P. Mohn, B. Johansson, Temperature-induced longitudinal spin fluctuations in Fe and Ni, *Phys. Rev. B Condens. Matter Mater. Phys.* 75 (2007) 1–7, <https://doi.org/10.1103/PhysRevB.75.054402>.
- [75] J.Y. Lee, Y.M. Koo, S. Lu, L. Vitos, S.K. Kwon, The behaviour of stacking fault energy upon interstitial alloying, *Sci. Rep.* 7 (2017) 17–22, <https://doi.org/10.1038/s41598-017-11328-4>.
- [76] P. Virtanen, R. Gommers, T.E. Oliphant, M. Haberland, T. Reddy, D. Cournapeau, E. Burovski, P. Peterson, W. Weckesser, J. Bright, S.J. van der Walt, M. Brett, J. Wilson, K.J. Millman, N. Mayorov, A.R.J. Nelson, E. Jones, R. Kern, E. Larson, C.J. Carey, I. Polat, Y. Feng, E.W. Moore, J. VanderPlas, D. Laxalde, J. Perktold, R. Cimrman, I. Henriksen, E.A. Quintero, C.R. Harris, A.M. Archibald, A. H. Ribeiro, F. Pedregosa, P. van Mulbregt, A. Vijaykumar, A. Pietro Baldelli, A. Rothberg, A. Hilboll, A. Kloekner, A. Scopatz, A. Lee, A. Rokem, C.N. Woods, C. Fulton, C. Masson, C. Häggström, C. Fitzgerald, D.A. Nicholson, D.R. Hagen, D. V. Pasechnik, E. Olivetti, E. Martin, E. Wieser, F. Silva, F. Lenders, F. Wilhelm, G. Young, G.A. Price, G.L. Ingold, G.E. Allen, G.R. Lee, H. Audren, I. Probst, J. P. Dietrich, J. Silteira, J.T. Webber, J. Slavić, J. Nothman, J. Buchner, J. Kulick, J. L. Schönberger, J. de Miranda Cardoso, J. Reimer, J. Harrington, J.L. Rodríguez, J. Nunez-Iglesias, J. Kuczynski, K. Tritz, M. Thoma, M. Newville, M. Kümmeler, M. Bolingbroke, M. Tartre, M. Pak, N.J. Smith, N. Nowaczyk, N. Shebanov, O. Pavlyk, P.A. Brodtkorb, P. Lee, R.T. McGibbon, R. Feldbauer, S. Lewis, S. Tygier, S. Sievert, S. Vigna, S. Peterson, S. More, T. Pudlik, T. Oshima, T.J. Pingel, T.P. Robitaille, T. Spura, T.R. Jones, T. Cera, T. Leslie, T. Zito, T. Krauss, U. Upadhyay, Y.O. Halchenko, Y. Vázquez-Baeza, SciPy 1.0: fundamental algorithms for scientific computing in Python, *Nat. Methods* 17 (2020) 261–272, <https://doi.org/10.1038/s41592-019-0686-2>.
- [77] P. Soven, Coherent-potential model of substitutional disordered alloys, *Phys. Rev.* 156 (1967) 809–813, <https://doi.org/10.1103/PhysRev.156.809>.
- [78] L. Vitos, I.A. Abrikosov, B. Johansson, Anisotropic lattice distortions in random alloys from first-principles theory, *Phys. Rev. Lett.* 87 (2001), 156401–156401–4, <https://doi.org/10.1103/PhysRevLett.87.156401>.
- [79] L. Vitos, Computational Quantum Mechanics for Materials Engineers - The EMTO Method and Applications, 1st ed., Springer, London, 2007 https://doi.org/10.1007/978-1-84628-951-4_5.
- [80] J.P. Perdew, K. Burke, M. Ernzerhof, Generalized gradient approximation made simple, *Phys. Rev. Lett.* 77 (1996) 3865–3868, <https://doi.org/10.1103/PhysRevLett.77.3865>.

- [81] L. Cheng, A. Böttger, T.H. de Keijser, E.J. Mittemeijer, Lattice parameters of iron-carbon and iron-nitrogen martensites and austenites, *Scr. Metall. Mater.* 24 (1990) 509–514, [https://doi.org/10.1016/0956-716X\(90\)90192-J](https://doi.org/10.1016/0956-716X(90)90192-J).
- [82] T.S. Hummelshøj, T.L. Christiansen, M. a J. Somers, Lattice expansion of carbon-stabilized expanded austenite, *Scr. Mater.* 63 (2010) 761–763, <https://doi.org/10.1016/j.scriptamat.2010.05.031>.
- [83] A.V. Ponomareva, Y.N. Gornostyrev, I.A. Abrikosov, Ab initio calculation of the solution enthalpies of substitutional and interstitial impurities in paramagnetic fcc Fe, *Phys. Rev. B Condens. Matter Mater. Phys.* 90 (2014) 1–13, <https://doi.org/10.1103/PhysRevB.90.014439>.
- [84] D. Molnár, S. Lu, S. Hertzman, G. Engberg, L. Vitos, Study of the alternative mechanism behind the constant strain hardening rate in highnitrogen steels, *Mater. Charact.* 170 (2020), <https://doi.org/10.1016/j.matchar.2020.110726>.
- [85] B.L. Gyorffy, A.J. Pindor, J. Staunton, G.M. Stocks, H. Winter, A first-principles theory of ferromagnetic phase transitions in metals, *J. Phys. F Met. Phys.* 15 (1985) 1337–1386, <https://doi.org/10.1088/0305-4608/15/6/018>.
- [86] L.M. Sandratskii, E.N. Kuvaldin, Band-theory approach to the study of local magnetization fluctuations in Fe and Ni, *J. Phys.: Codens. Matter* 3 (1991) 7663–7682.
- [87] Z. Dong, S. Schönecker, W. Li, S.K. Kwon, L. Vitos, Plastic deformation modes in paramagnetic γ -Fe from longitudinal spin fluctuation theory, *Int. J. Plast.* 109 (2018) 43–53, <https://doi.org/10.1016/j.ijplas.2018.05.007>.
- [88] W. Li, S. Lu, Q.M. Hu, B. Johansson, S.K. Kwon, M. Grehk, J.Y. Johnsson, L. Vitos, Generalized stacking fault energy of γ -Fe, *Philos. Mag.* 96 (2016) 524–541, <https://doi.org/10.1080/14786435.2016.1140912>.
- [89] G. Kresse, J. Hafner, Ab initio molecular dynamics for liquid metals, *Phys. Rev. B* 47 (1993) 558–561, <https://doi.org/10.1103/PhysRevB.47.558>.
- [90] G. Kresse, J. Furthmüller, Efficient iterative schemes for ab initio total-energy calculations using a plane-wave basis set G, *Phys. Rev. B* 54 (1996) 11169–11186, <https://doi.org/10.1021/acs.jpcsa.0c01375>.
- [91] W. Kohn, N. Rostoker, Solution of the schrödinger equation in periodic lattices with an application to metallic lithium, *Phys. Rev.* 94 (1954) 1111–1120, <https://doi.org/10.1103/PhysRev.94.1111>.
- [92] J. Korringa, On the calculation of the energy of a bloch wave in a metal, *Physica* (1947) 392–400.
- [93] E. Pereloma, D. Cortie, N. Singh, G. Casillas, F. Niessen, Uncovering the mechanism of dislocation interaction with nanoscale (<4nm) interphase precipitates in microalloyed ferritic steels, *Mater. Res. Lett.* 8 (2020) 341–347, <https://doi.org/10.1080/21663831.2020.1764121>.
- [94] J. Von Appen, R. Dronskowski, Carbon-induced ordering in manganese-rich austenite - A density-functional total-energy and chemical-bonding study, *Steel Res. Int.* (2011) 101–107, <https://doi.org/10.1002/srin.201000260>.
- [95] B. Wang, K.V. Werner, M. Villa, T.L. Christiansen, M.A.J. Somers, Phase stability and deformation modes in functionally graded metastable austenitic stainless steel; a novel approach to evaluate the role of nitrogen, *Metall. Mater. Sci.* (2022), <https://doi.org/10.1007/s11661-022-06904-x>.
- [96] T. Hickel, S. Sandlöbes, R.K.W. Marceau, A. Dick, I. Bleskov, J. Neugebauer, D. Raabe, Impact of nanodiffusion on the stacking fault energy in high-strength steels, *Acta Mater.* 75 (2014) 147–155, <https://doi.org/10.1016/j.actamat.2014.04.062>.
- [97] V.G. Gavriljuk, V.N. Shvanyuk, B.D. Shanina, Change in the electron structure caused by C, N and H atoms in iron and its effect on their interaction with dislocations, *Acta Mater.* 53 (2005) 5017–5024, <https://doi.org/10.1016/j.actamat.2005.07.028>.
- [98] R. Xie, S. Lu, W. Li, Y. Tian, L. Vitos, Dissociated dislocation-mediated carbon transport and diffusion in austenitic iron, *Acta Mater.* 191 (2020) 43–50, <https://doi.org/10.1016/j.actamat.2020.03.042>.
- [99] J.B. Seol, B.H. Lee, P. Choi, S.G. Lee, C.G. Park, Combined nano-SIMS/AFM/EBSD analysis and atom probe tomography, of carbon distribution in austenite/ ϵ -martensite high-Mn steels, *Ultramicroscopy* 132 (2013) 248–257, <https://doi.org/10.1016/j.ultramic.2013.01.009>.
- [100] S.D.L. Williamson, I. Ivanov, R. Weic, P.J. Wilbure, Role of chromium in high-dose, high-rate, elevated temperature nitrogen implantation of austenitic stainless steels, *MRS Proc.* (1992) 473–478.
- [101] H.L. Che, T.L. Christiansen, M.K. Lei, M.A.J. Somers, Co-existence of $\gamma'N$ phase and γN phase in nitrided austenitic Fe-Cr-Ni alloys - II: a pragmatic modeling approach, *Acta Mater.* 235 (2022), <https://doi.org/10.1016/j.actamat.2022.118094>.
- [102] B. Yin, S. Yoshida, N. Tsuji, W.A. Curtin, Yield strength and misfit volumes of NiCoCr and implications for short-range-order, *Nat. Commun.* 11 (2020), <https://doi.org/10.1038/s41467-020-16083-1>.
- [103] J. Talonen, H. Hänninen, Formation of shear bands and strain-induced martensite during plastic deformation of metastable austenitic stainless steels, *Acta Mater.* 55 (2007) 6108–6118, <https://doi.org/10.1016/j.actamat.2007.07.015>.
- [104] G. Cios, T. Tokarski, A. Źywczak, R. Dziurka, M. Stępień, M. Marciszko Gondek, B. Pawłowski, K. Wieczerek, P. Bała, The investigation of strain-induced martensite reverse transformation in AISI 304 austenitic stainless steel, *Metall. Mater. Trans. A Phys. Metall. Mater. Sci.* 48 (2017) 4999–5008, <https://doi.org/10.1007/s11661-017-4228-1>.
- [105] Y. Tian, O.I. Gorbato, A. Borgenstam, A.V. Ruban, P. Hedström, Deformation microstructure and deformation-induced martensite in austenitic Fe-Cr-Ni alloys depending on stacking fault energy, *Metall. Mater. Trans. A Phys. Metall. Mater. Sci.* 48 (2017) 1–7, <https://doi.org/10.1007/s11661-016-3839-2>.
- [106] B. Wang, C. Hong, G. Winther, T.L. Christiansen, M.A.J. Somers, Deformation mechanisms in meta-stable and nitrogen-stabilized austenitic stainless steel during severe surface deformation, *Materialia (Oxf)* 12 (2020), 100751, <https://doi.org/10.1016/j.mtla.2020.100751>.
- [107] E.D. Butakova, K.A. Malyshev, N.I. Noskova, Stacking fault energy in iron-nickel and iron-nickel-chromium alloys, *Fiz. Met. Metalloved.* 35 (1973) 662–664.
- [108] R. Fussik, G. Egels, W. Theisen, S. Weber, Stacking fault energy in relation to hydrogen environment embrittlement of metastable austenitic stainless crni-steels, *Met. (Basel)* (2021) 11, <https://doi.org/10.3390/met1108110>.
- [109] J.F.A. Borges, A.F. Padilha, K. Imakura, Determinação da energia de defeito de empilhamento por difratometria de raios-x em metais CFC, in: 37th Reunião Anual Da Sociedade Brasileira Para o Progresso Da Ciencia, 1985, pp. 1–12.
- [110] S.W. Yang, J.E. Spruiell, Cold-worked state and annealing behaviour of austenitic stainless steel, n.d.
- [111] A.E. Pontini, J. Daniel Hermida', X-ray diffraction measurement of the stacking fault energy reduction induced by hydrogen in an AISI 304 steel, 1997.
- [112] R.M. Latanision, A.W. Ruff, the temperature dependence of stacking fault energy in Fe-Cr-Ni alloys, *Metall. Trans. 2* (1971) 505–509.
- [113] L.E. Murr, Stacking-fault anomalies and the measurement of stacking-fault free energy in fcc thin films, *Thin Solid Films* 4 (1969) 389–412.
- [114] T. Yonezawa, K. Suzuki, S. Ooki, A. Hashimoto, The effect of chemical composition and heat treatment conditions on stacking fault energy for Fe-Cr-Ni austenitic stainless steel, *Metall. Mater. Trans. A Phys. Metall. Mater. Sci.* 44 (2013) 5884–5896, <https://doi.org/10.1007/s11661-013-1943-0>.
- [115] Y. Kaneko, PhD Thesis, Nagoya University, 1996.
- [116] L.M. Brown, The self-stress of dislocations and the shape of extended nodes, *Philos. Mag.* 10 (1964) 441–466, <https://doi.org/10.1080/14786436408224223>.
- [117] P.C.J. Gallagher, The influence of alloying, temperature, and related effects on the stacking fault energy, *Metall. Mater. Trans. B* 1 (1970) 2429–2461, <https://doi.org/10.1007/BF03038370P.C.J>.